SPECIAL IPWG-7 COLLECTION

Understanding Overland Multisensor Satellite Precipitation Error in TMPA-RT Products

ABEBE SINE GEBREGIORGIS,[a,b] PIERRE-EMMANUEL KIRSTETTER,[a,b,c] YANG E. HONG,[a,b,c] NICHOLAS J. CARR,[b,d] JONATHAN J. GOURLEY,[c] WALT PETERSEN,[e] AND YAOYAO ZHENG[b,d]

[a] *School of Civil Engineering and Environmental Sciences, University of Oklahoma, Norman, Oklahoma*
[b] *Advanced Radar Research Center, University of Oklahoma, Norman, Oklahoma*
[c] *NOAA/National Severe Storms Laboratory, Norman, Oklahoma*
[d] *School of Meteorology, University of Oklahoma, Norman, Oklahoma*
[e] *NASA Marshall Space Flight Center, Huntsville, Alabama*

(Manuscript received 17 October 2015, in final form 4 November 2016)

ABSTRACT

The Tropical Rainfall Measuring Mission (TRMM) Multisatellite Precipitation Analysis (TMPA) has provided the global community a widely used multisatellite (and multisensor type) estimate of quasi-global precipitation. One of the TMPA level-3 products, 3B42RT/TMPA-RT (where RT indicates real time), is a merged product of microwave (MW) and infrared (IR) precipitation estimates, which attempts to exploit the most desirable aspects of both types of sensors, namely, quality rainfall estimation and spatiotemporal resolution. This study extensively and systematically evaluates multisatellite precipitation errors by tracking the sensor-specific error sources and quantifying the biases originating from multiple sensors. High-resolution, ground-based radar precipitation estimates from the Multi-Radar Multi-Sensor (MRMS) system, developed by the National Severe Storms Laboratory (NSSL), are utilized as reference data. The analysis procedure involves segregating the grid precipitation estimate as a function of sensor source, decomposing the bias, and then quantifying the error contribution per grid. The results of this study reveal that while all three aspects of detection (i.e., hit, missed-rain, and false-rain biases) contribute to the total bias associated with IR precipitation estimates, overestimation bias (positive hit bias) and missed precipitation are the dominant error sources for MW precipitation estimates. Considering only MW sensors, the TRMM Microwave Imager (TMI) shows the largest missed-rain and overestimation biases (nearly double that of the other MW estimates) per grid box during the summer and winter seasons. The Special Sensor Microwave Imagers/Sounders (SSMIS on board *F17* and *F16*) also show major error during winter and spring, respectively.

1. Introduction

Precipitation is a vital component of the water cycle, connecting Earth's surface and atmosphere. It is also a major input for many hydrological models, as it is the driving force behind all hydrologic processes on Earth's surface. Accurate information regarding the frequency and quantity of precipitation enables a better understanding of Earth's water cycle. In the modern era, spaceborne platforms have provided insights on the character of global-scale precipitation. Consequently, an improved understanding of the error structure of satellite precipitation estimates at quasi-global scale is particularly pertinent from a scientific perspective and would be valuable for numerous hydrometeorological applications such as quantitative precipitation forecasting and numerical weather prediction models (Turk et al. 1999), flood forecasting and water resources monitoring (Hong et al. 2007a; Gebregiorgis and Hossain 2011, 2013), land data assimilation (Gottschalck et al. 2005; Tian et al. 2007), and landslide prediction (Hong et al. 2007b).

Precipitation is traditionally measured using various types of rain gauges. Rain gauges provide direct (in situ) measurements of precipitation, but the spatial distribution and density of rain gauge networks is typically far too coarse to capture the spatial variability of precipitation at small scales. Moreover, there are very few rain gauges whose data are available in real time and at high enough

Corresponding author e-mail: Abebe Sine Gebregiorgis, abesine@ou.edu; abesine2002@gmail.com

DOI: 10.1175/JHM-D-15-0207.1

© 2017 American Meteorological Society. For information regarding reuse of this content and general copyright information, consult the AMS Copyright Policy (www.ametsoc.org/PUBSReuseLicenses).

Brought to you by NOAA Central Library | Unauthenticated | Downloaded 09/27/21 03:56 PM UTC

TABLE 1. List of satellite sensors contributing to TMPA-RT (Huffman and Bolvin 2015). Scan patterns are conical (CN) or cross track (CT). In the sensor column, SSM/I-*F13*, SSM/I-*F14*, and SSM/I-*F15* refer to SSM/I on board *F13*, *F14*, and *F15*, respectively. AMSU-B/*15*, AMSU-B/*16*, and AMSU-B/*17* refer to AMSU-B on board *NOAA-15*, *NOAA-16*, and *NOAA-17*, respectively. MHS-*18* and MHS-*19* refer to MHS on board *NOAA-18* and *NOAA-19*, respectively.

Sensor	Agency	Start date	End date	Swath width (km)	Scan pattern
AMSR-E	NASA	19 Jun 2002	3 Oct 2011	1445	CN
SSM/I-*F13*	DMSP	17 Feb 2000	31 Jul 2009	1394	CN
SSM/I-*F14*	DMSP	17 Feb 2000	23 Aug 2008	1394	CN
SSM/I-*F15*	DMSP	23 Feb 2000	13 Aug 2006	1394	CN
SSMIS-*F16*	DMSP	20 Nov 2005	Present	1707	CN
SSMIS-*F17*	DMSP	19 Mar 2008	Present	1707	CN
SSMIS-*F18*	DMSP	8 Mar 2010	Present	1707	CN
AMSU-B/*15*	NOAA	17 Feb 2000	14 Sep 2010	2178.8	CT
AMSU-B/*16*	NOAA	4 Oct 2000	30 Apr 2010	2178.8	CT
AMSU-B/*17*	NOAA	28 Jun 2002	17 Dec 2009	2178.8	CT
MHS-*18*	NOAA	25 May 2005	Present	2348	CT
MHS-*19*	NOAA	9 Mar 2009	Present	2348	CT
MetOp-A	ESA/EUMETSAT	5 Dec 2006	Present	2348	CT
MetOp-B	ESA/EUMETSAT	15 Aug 2013	Present	2348	CT
TMI	NASA	27 Nov 1997	8 Apr 2015	759	CN
IR GOES	NOAA/CPC 4 km T_b	17 Feb 2000	Present	>3000	

frequency for hydrologic applications such as flash flood forecasting. Alternatively, radar, which is generally only available in the developed nations of the world, provides an indirect measurement of precipitation with relatively high spatiotemporal resolution. The useful range of radar precipitation estimates extends to a few hundred kilometers of the radar site, but the coverage of radars is limited in mountainous regions because of beam blockage and in case of shallow, cool season precipitation systems. Good accuracy of the terrestrial sensors primarily stems from the nature of measurement, that is, direct measurement with gauges or active remote sensing with radars. Radar reflectivity provides information about the size and number density of hydrometeors at multiple levels in the atmosphere (Kirstetter et al. 2013). Radar instruments have also been flown on board satellites for precipitation measurement missions. For instance, the Tropical Rainfall Measuring Mission (TRMM) Precipitation Radar (PR) operating at 13.8 GHz provides the vertical structure of precipitation systems for the investigation of its three-dimensional structure, obtaining quantitative measurements over land and ultimately improving rainfall estimation (Iguchi et al. 2000). Its successor, the Dual-Frequency Precipitation Radar (DPR) on board the Global Precipitation Measurement (GPM) mission's core satellite, is designed to provide more detailed rain/snow information, including light rainfall and snowfall in high-latitude regions (Hou et al. 2014; Huffman et al. 2015). The *CloudSat* radar observes the cloud condensate and precipitation (Stephens et al. 2002). Alternatively, most spaceborne precipitation estimation relies upon passive sensors, which provide more indirect information than either gauges or radar but have the advantage of complete coverage in remote regions such as over oceans, mountainous regions, and sparsely populated areas where other sources of precipitation data are not available. Consequently, satellite precipitation estimates are particularly useful for identifying hydrometeorological hazards arising from smaller-scale precipitation features occurring in sparsely instrumented areas. However, gauges and radars estimate precipitation from Earth's surface and are therefore expected to provide estimates with better accuracy than orbiting spaceborne sensors.

A plethora of satellite precipitation products is currently available, and some of the most commonly used are blended products, which merge precipitation estimates from microwave (MW) and infrared (IR) sensors. One of the most popular multisatellite products, the TRMM Multisatellite Precipitation Analysis–real time (TMPA-RT) algorithm, combines multiple independent precipitation estimates from the TRMM Microwave Imager (TMI; Kummerow et al. 1998; McCollum and Ferraro 2003), Advanced Microwave Scanning Radiometer for Earth Observing System (AMSR-E; Shibata et al. 2003; Turk and Miller 2005; McCollum and Ferraro 2003), Special Sensor Microwave Imager (SSM/I; Ferraro 1997; Hollinger et al. 1990), Special Sensor Microwave Imager/Sounder (SSMIS; Sun and Weng 2008), Advanced Microwave Sounding Unit (AMSU; Vila et al. 2007), Microwave Humidity Sounder (MHS; Ferraro et al. 2005), and microwave-adjusted merged geo-infrared (Huffman et al. 2010; Hsu et al. 1997). The sensors contributing to the TMPA-RT algorithm are presented in Table 1, and the reader is also referred to Huffman and Bolvin (2015) for more details.

Brought to you by NOAA Central Library | Unauthenticated | Downloaded 09/27/21 03:56 PM UTC

Satellite precipitation products are generated from different algorithm processing levels (Hou et al. 2008). Level-1 products provide instrument data at full resolution (at sensor footprint scales) and reconstructed and calibrated radiance/reflectivity swath data with the computed Earth location. In the case of level-2 products, the physical parameters in full resolution are derived preserving the orbital structure. In the TRMM case, these parameters include the TMI hydrometeor profile, the PR surface cross section, rain characteristics, rainfall rate, and profile. The TRMM level-3 products are generally derived from the level-2 products. These products are space- and/or time-averaged data, which are mapped onto grids. Consequently, the grid precipitation estimate associated with a TRMM level-3 satellite precipitation product could originate from either a single sensor estimate (MW or IR) or from an average of two or more sensors' estimates. This framework allows the retrieval algorithm to utilize all the available information and exploit the advantages of each sensor or type of sensor (e.g., Hsu et al. 1997; Joyce et al. 2004; Huffman et al. 2007, 2010). On the other side, the uncertainty, which propagates to the level-3 TRMM product, is also the combined result of all the errors related to these algorithmic processes, and it includes both retrieval and sampling errors.

To advance the usefulness of satellite precipitation estimates for hydrometeorological applications, an improved understanding of the sensor-specific error characteristics (hereafter used interchangeably with uncertainty) associated with these multisensor precipitation estimates is required. Several attempts have been made to quantify the uncertainty of the TMPA-RT products (e.g., Adler et al. 2001; Gottschalck et al. 2005; Ebert et al. 2007; Tian and Peters-Lidard 2007; Tian et al. 2007, 2009; Sapiano and Arkin 2009; Kubota et al. 2009; Tian et al. 2010; Tian and Peters-Lidard 2010; Gebregiorgis and Hossain 2014, 2015; Tang et al. 2014). For instance, Tang et al. (2014) validated precipitation retrievals (level-2 products) from 12 passive MW radiometers independently using high-resolution ground-based radar data at the instantaneous time scale. Their results revealed that all MW radiometers overestimate and underestimate precipitation during the summer and winter seasons, respectively. Their study also revealed that the imager products perform (relatively) better than the sounder products. The majority of the previous studies focus on the overall error of the TRMM level-3 rain products. In general, the overall error convolves various aspects such as detection and quantification of precipitation from a variety of sensors with different capabilities. The original intent of the present analysis is to track the contribution of each sensor to the combined product in order to provide better feedback to the combined algorithm developers, highlight the performance of satellite-only rainfall estimate, and ultimately improve the precipitation products.

Because a posteriori gauge correction alters the contribution of each sensor and makes diagnostic approach difficult, the focus is on the satellite-only 3B42RT (where RT stands for real time) product. To better understand the nature of uncertainty propagation from level-2 to level-3 products, first the uncertainty contributed by each individual sensor or group of sensors in the level-3 product should be characterized and quantified. Therefore, the primary goal of this study is to quantify the magnitude of the error contributed by individual/a group of sensor estimates to the merged level-3 TRMM product. Since the current GPM algorithm is built up on the success of TRMM with almost the same sensor configurations, the results of this work are also expected to be valuable in improving our understanding of error structures in Integrated Multi-satellite Retrievals for GPM (IMERG) precipitation estimates (Huffman et al. 2015).

This paper is organized in five sections. Section 2 provides information about the study region and a description of the satellite and ground-based radar data used in this study; section 3 details the study methodology; and section 4 presents the results and specifically discusses the accuracy of spatial and temporal variation of satellite and reference data, the error structure associated with the level-3 TRMM product (3B42RT), and the contribution of error from the individual sensor estimates. Finally, section 5 summarizes significant findings and lists potential future research directions.

2. Study region and datasets

a. Description of the study domain and reference precipitation data

The implementation of weather radar networks over North America, specifically, the Next Generation Weather Radar (NEXRAD) network over the United States, has greatly improved our ability to monitor and measure surface precipitation (Crum et al. 1993). Because of the availability of high-quality radar reference data, this study was conducted over the contiguous United States (CONUS). The CONUS comprises diverse topography that ranges from 0 (South and East Coast regions) to 4500 m (Intermountain West) above mean sea level. Moreover, the region's diverse topographic nature (ranging from lowland and flat flood plains to high mountains), diverse climatic zones, diverse land use and land cover, and a wide array of precipitation systems (tropical and midlatitude cyclones, airmass thunderstorms, orographic precipitation, supercells, etc.)

Brought to you by NOAA Central Library | Unauthenticated | Downloaded 09/27/21 03:56 PM UTC

make the study area a good test bed for evaluating the performance of satellite precipitation algorithms.

The reference precipitation dataset used in this study is composed of high-resolution ground radar products from the NOAA/National Severe Storms Laboratory's (NSSL) Multi-Radar Multi-Sensor (MRMS) system (Zhang et al. 2016). MRMS combines information from all ground-based radars to obtain radar-based precipitation estimates at high spatial and temporal resolutions (0.01°/2 min). It exploits the overlapping coverage of the WSR-88D network and the level-2 satellite data feeds to build a seamless rapidly updating, high-resolution 3D cube of radar data. Objectively, it blends volumetric radar data with surface, upper air, lightning, rain gauges, and model analysis fields to produce severe weather products. For the purpose of quality control, the dataset includes a radar quality index (RQI; Zhang et al. 2016), which ranges from 0% to 100% (with 100% corresponding to the highest quality). The RQI provides some information about the uncertainty of the radar precipitation estimate resulting from radar beam sampling characteristics (i.e., beam blockage, height, and width) and their relationship with respect to the vertical precipitation profile (Zhang et al. 2011). Chen et al. (2013) quantitatively related the RQI to errors in the MRMS daily rainfall totals for different regions in the CONUS. The MRMS product used in this study is a gauge-adjusted radar product at the hourly time scale. Similarly to Kirstetter et al. (2012), a quantitative filtering is applied in case of significant discrepancy between radar and gauges at the hourly time steps, with discarding instances where grid-by-grid ratios between the hourly gauge-adjusted and the hourly radar-only products are outside the 0.1–10 range. Hourly snow occurrence and RQI products are also specifically derived for satellite evaluation purposes (http://wallops-prf.gsfc.nasa.gov/NMQ/Docs/DailyProducts.pdf). These products are then aggregated from their native resolution (1 km/1 h) to the TMPA resolution (25 km/3 h) for comparison grid by grid. As mentioned in previous studies (Kirstetter et al. 2015; Carr et al. 2015), it is important to emphasize the quality in the reference dataset in an attempt to evaluate and understand the nature of satellite rainfall error structure. Without high-quality reference data, it is unlikely to perform proper assessments and draw meaningful conclusions about the error structures in satellite rainfall products. To achieve the objective of this study, we limit the comparisons to locations that have the highest radar quality index (i.e., RQI = 100%), in order to minimize the impact of errors in the reference datasets on the analysis. Understandably, applying this conditioning shrinks the amount of data, which varies from time to time: minimum during the summer and maximum in winter. On average, the data have been reduced by 38% during the entire study period. Three-hourly accumulations of the MRMS gauge-adjusted radar product are used hereafter for the evaluation of the TMPA product.

b. *Satellite precipitation data*

The primary types of precipitation sensors that contribute to the TRMM level-3 product can be partitioned into three categories: IR imagers, passive microwave (PMW) radiometers, and the TRMM PR (Kummerow et al. 1998). Basically, all these types of sensors are on board the low-Earth-orbiting TRMM satellite and are designed to provide both independent information along with the combined products. The Visible and Infrared Scanner (VIRS) on board TRMM does not provide precipitation information directly as it is less reliable; rather, it provides the cloud-top temperature and structures to support the description obtained by the MW sensors. Moreover, visible and infrared (VIS/IR) data from the geostationary satellite platforms provide frequent and longer time series data that serve an important role in filling the gaps due to infrequent MW observations. The VIS/IR data processing first discriminates the brightness of the cloud in the visible spectrum and/or the low temperature of the cloud top as seen in the thermal spectrum (Arkin and Meisner 1987). Then it evaluates further criteria such as cloud area extent, time history or evolutionary information, and textural features to correlate with the rainfall estimates (Adler and Negri 1988).

Microwave instruments can provide observations of cloud and precipitation properties, beyond simple cloud-top quantities. Microwave sensors can be classified as either active (i.e., radar), passive radiometric imagers, or sounders (Ferraro et al. 2005). The active sensors emit their own source of electromagnetic radiation and observe the direct backscattered microwave radiation from hydrometeors (or other scatterers). Passive microwave radiometers measure the intensity (expressed as brightness temperatures) of upwelling microwave radiation from Earth's surface and atmosphere. Radiometers can operate in imaging or sounding modes and are consequently referred to as imagers and sounders, respectively. While the radiometric imagers measure and map sea surface, cloud-top, and land surface temperature by scanning across segments of Earth's surface and atmosphere, the sounders provide vertical atmospheric temperature and moisture profiles and quantitative images of meteorological variables such as total precipitable water by making vertical soundings of the atmosphere (Weng et al. 2003). The precipitation sensor types used by different satellite missions over the

Brought to you by NOAA Central Library | Unauthenticated | Downloaded 09/27/21 03:56 PM UTC

last 15 years are summarized in Table 1. The sensors used in precipitation estimation over the CONUS during the study period (2013/14) are identified as TMI; SSMIS on board *F16*, *F17*, and *F18* (hereafter referred to as SSMIS-*F16*, SSMIS-*F17*, and SSMIS-*F18*, respectively); MHS; *MetOp-B*; AMSU–MHS average; conical average (as per the scan pattern given in Table 1); and IR (Huffman and Bolvin 2015).

Because of the complimentary nature of IR and MW sensors, the final satellite precipitation product (level 3) is ultimately produced by merging the precipitation estimates originating from multiple satellite sensors (Huffman et al. 2007). The MW and combined radar–radiometer estimates are more accurate because of the more physically direct relationships that exist between the precipitation properties and the measured satellite variables (i.e., MW brightness temperatures or backscattered radar reflectivity; Kidd et al. 2003). However, the principal drawback associated with MW products is their low temporal sampling frequency, resulting from their low-Earth orbits. On the other hand, precipitation estimates from IR sensors generally have lower accuracies because of the more ambiguous relationship between cloud-top temperature (the measured quantity) and precipitation properties. However, the IR sensors provide more frequent coverage because of their geosynchronous orbits. By exploiting these complimentary advantages, the merging of precipitation estimates from multiple sensors significantly improves the spatial and temporal scales of the final level-3 product. First, the rain rates from the TRMM combined algorithm (2B31) based on both PR and TMI estimates are used to calibrate all available microwave precipitation estimates from the TMI, SSMIS, SSM/I, AMSR-E, and AMSU-B radiometers using a histogram matching method to produce microwave-based precipitation estimates (Huffman et al. 2007). IR precipitation estimates from geostationary platforms are also calibrated using the TRMM data. Finally, the two precipitation estimates are merged together to produce the level-3 TRMM (3B42RT) product. Naturally, the uncertainty inherited in the level-3 satellite precipitation estimates results from a combination of the uncertainties associated with all contributing sensors' retrieval algorithms.

In this study, the sources (sensors or types of sensors) contributing to the grid's precipitation estimate have been identified at the final level-3 product resolutions (0.25°/3 h). To determine the sensor source and ultimate contribution to the uncertainty in the final level-3 precipitation product, it is first important to understand the space–time coverage of the sensors defining their contribution to the TMPA product over the CONUS. Figure 1 shows the spatial percentage of contribution from each sensor listed in Table 1 during the 2-yr study period (from 2 January 2013 to 31 December 2014) along with the spatial coverage of the reference (radar) data. The percentage contribution is the frequency in which the grid's rainfall estimates originated from the specific sensor type during the 2-yr period. In general, the sampling frequencies of the SSMIS-*F17* and *MetOp-B* sensors are lower over the entire United States (less than 10%) than the other sensors. For TMI and SSMIS-*F18*, the sampling size ranges between 5% and 20%. Note that, given the orbit of TRMM, the spatial coverage of TMI is limited to the subtropical region of the CONUS. MHS on board the NOAA series satellites has a slightly wider swath (2348 km, Table 1) and thus provides good spatial (western, southern, and eastern parts of the United States) and temporal coverage (up to 30%). In case of TMPA-RT, the rainfall estimates primarily come from MW information and then use MW-calibrated IR data to fill the gaps in the MW coverage. Therefore, the IR contribution depends on the extent of MW contribution. In general, the IR contributes less over the midwestern region of the CONUS and more over certain parts of the northern and southeastern regions. The reference dataset (MRMS) has moderately good sampling frequency in the central and eastern parts of the United States, with its maximum coverage in the southern part of the study region. MRMS's coverage is considerably spottier over the Intermountain West (Maddox et al. 2002). This spatial coverage pattern is expected as the RQI is highest when 1) the radar beam is unobstructed (i.e., not blocked by terrain or buildings), 2) the radar beam is low in the atmosphere (generally near the radar site), and 3) when the radar beam is below the freezing level (which occurs most often when the freezing level is high during warm season months).

Figure 2 highlights the temporal variability of percentage of area contribution for MW and IR sensors over the CONUS. In general, the IR contribution over the United States is relatively high during the winter season of 2013/14 (reaches up to 60% in February), whereas the MW coverage is high from April to November (with nearly 90% area coverage from June to September). We speculate that the lesser MW contribution during the winter is related to the presence of snow and ice cover and weakly scattered MW radiation during this period. In other words, the emissivity signal from the terrestrial snow and ice cover impacts on the measured MW signals during winter, challenging the extraction of the signal from precipitation.

Figure 3 provides information regarding the area coverage associated with individual MW sensors for the months of August 2013 and January 2014. These two months were chosen to show a representative month

Brought to you by NOAA Central Library | Unauthenticated | Downloaded 09/27/21 03:56 PM UTC

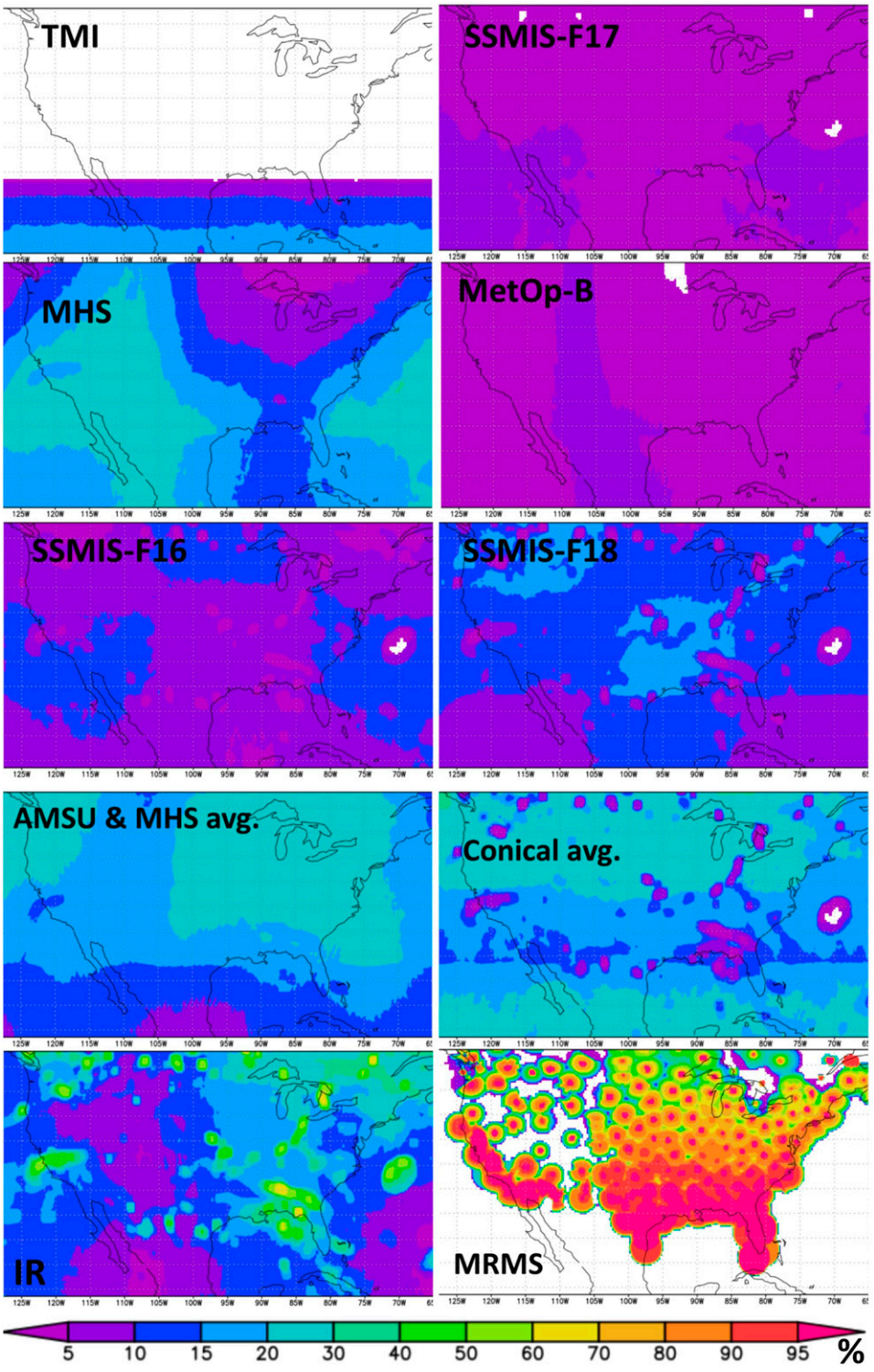

FIG. 1. Percentage of spatial coverage for MW, IR, and high-quality MRMS QPE during the period of 2013/14. The percentage for each grid box is computed by dividing the number of samples of individual sensor by the total number of observation during the study period.

Brought to you by NOAA Central Library | Unauthenticated | Downloaded 09/27/21 03:56 PM UTC

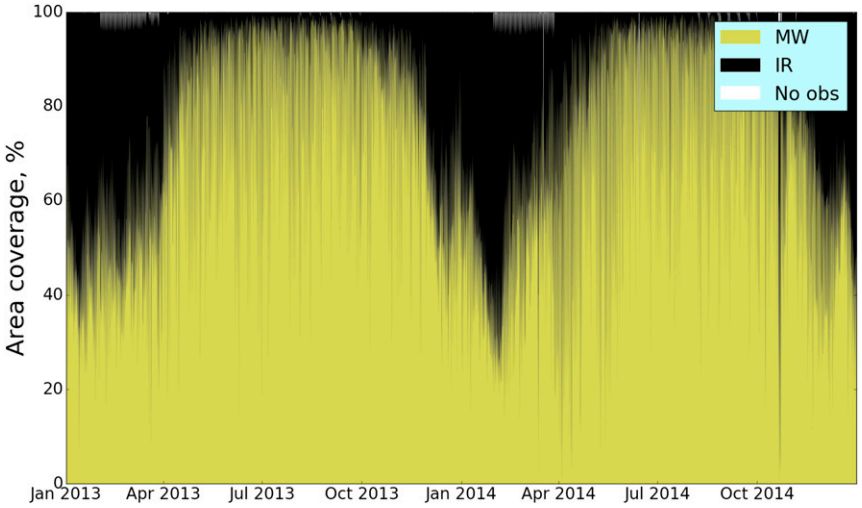

FIG. 2. Percentage of area coverage for MW and IR sensors over the CONUS during the period of 2013/14. The number of grid boxes sampled by individual sensors is divided by the total number of grid boxes over CONUS.

during the summer and winter seasons. In general, TMI, MHS, SSMIS-*F18*, the AMSU–MHS average, and the conical average are the dominant contribution for grid precipitation estimation. Generally the area coverage of the MW sensors is consistent in both months, except for the TMI and MHS sensors. Specifically, the TMI has somewhat higher area coverage in the month of January than August and vice versa for the MHS. The basic feature that we can observe from this plot is the use of some sensors in the absence of others (i.e., in a gap-filling way). For instance, whenever TMI is not available, the gap is mainly covered by MHS, while the AMSU–MHS average substitutes for the conical average when it is not available. In summary, the sensor combinations basically depend on the scan pattern and the orbit of the platform.

3. Procedure and methodology

The flowchart of the methodology and procedure followed in this study is presented in Fig. 4. We utilized three different level-3 TMPA-RT products: 3B40RT, which is high-quality pure MW rainfall estimates; 3B41RT single IR sensor product, which is calibrated by high-quality MW rainfall estimates; and 3B42RT, which is the merged product of MW and IR estimates. The source of rainfall estimates (sensors type) is also included in the data field.

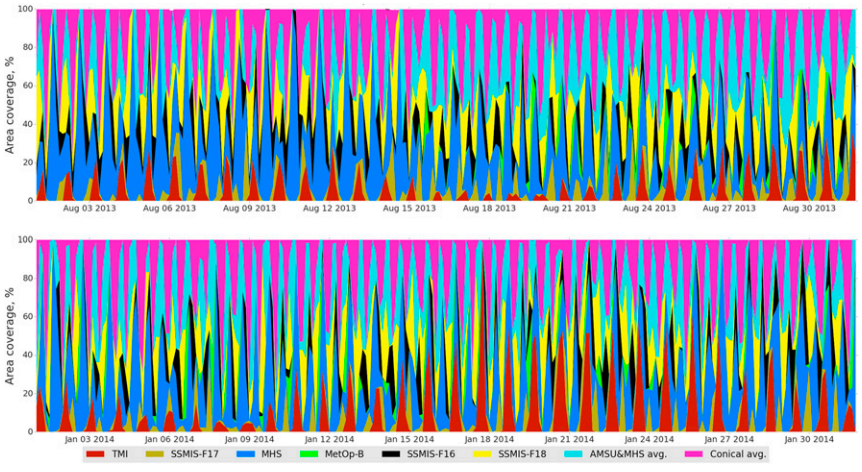

FIG. 3. Percentage of area coverage for MW sensors over the United States during (top) August 2013 and (bottom) January 2014.

Brought to you by NOAA Central Library | Unauthenticated | Downloaded 09/27/21 03:56 PM UTC

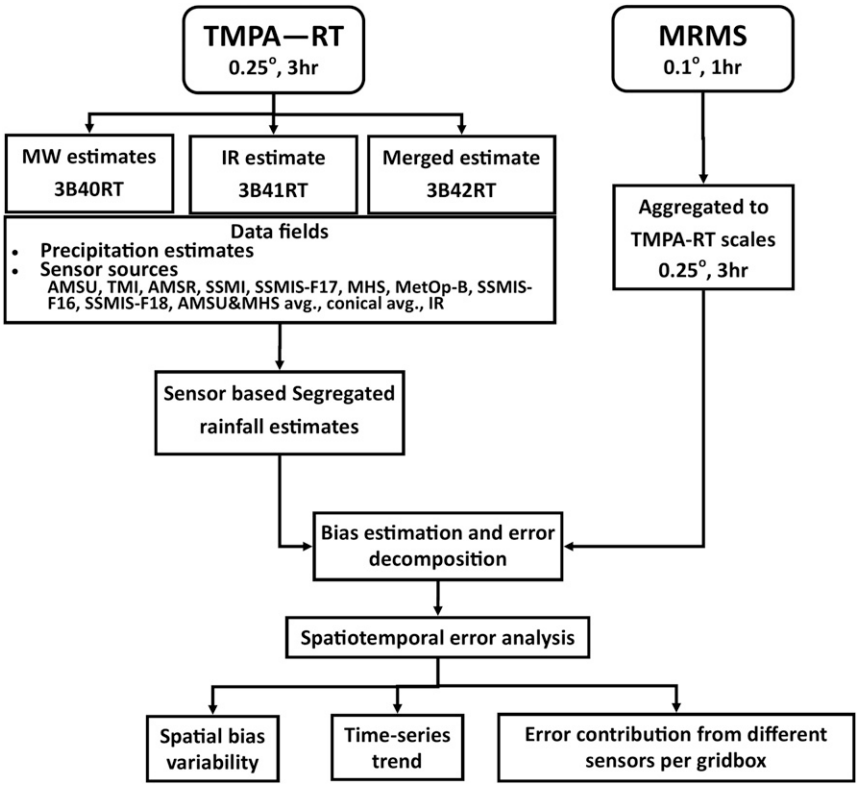

FIG. 4. Flowchart of the procedure used in this study. The lhs shows how sensor information is extracted from three different level-3 TMPA-RT products. The 3B40RT (pure MW estimates) and 3B42RT (merged estimates) data fields include precipitation estimates and the sensors type for each grid box at each time step, which helps to segregate the estimates as a function of sensor types. The rhs indicates the aggregation of MRMS (reference data) from its native spatiotemporal resolutions to TMPA-RT scales for bias estimation and error decomposition.

The rainfall estimates and sensor information were extracted from the data field of the three products. Based on the sensor type, the rainfall estimates for each grid box were separated into nine groups. In some cases, the rainfall estimate of a single grid box is derived from an individual sensor and is treated independently. In other cases, the rainfall estimate results from an averaging of two or more sensors. As an example, the AMSU–MHS average is the pixel-weighted average of AMSU-B and MHS estimates. Conical average is the pixel-weighted average of calibrated conical-scan microwave radiometer estimates of TMI, SSM/I, SSMIS, and AMSR. As seen on the right side of the flowchart, the reference data (MRMS) were aggregated from their native resolution (0.1°/1 h) to TMPA-RT (0.25°/3 h) scales.

The bias estimation and error decomposition scheme (Tian et al. 2009) was implemented at the individual grid level. The error decomposition scheme is utilized to separate the precipitation retrieval errors into three independent components: hit/estimation bias, missed-rain bias, and false-rain bias. A hit bias occurs when the rainfall is detected successfully by the satellite but is not estimated accurately; negative hit bias indicates underestimation and is positive for overestimation. There are circumstances whereby the satellite does not detect the rainfall while there is actual rain on the ground and vice versa. Such circumstances are called missed-rain and false-rain bias, respectively. This error decomposition scheme helps to relate a sensor to an error component and its relative contribution. Such detailed error analysis also provides useful feedback to level-2 and level-3 algorithm developers. Often, physically based precipitation retrieval algorithms utilized by MW sensors (e.g., GPROF 2010) involve two major processes: screening for precipitation (precipitation detection) and rain-rate estimation (precipitation quantification; Smith et al. 1998). During the screening (precipitation detection) stage, MW sensors detect precipitation by utilizing both the emission of MW radiation by liquid hydrometeors (generally over oceans) and scattering of MW radiation by ice-phase

Brought to you by NOAA Central Library | Unauthenticated | Downloaded 09/27/21 03:56 PM UTC

hydrometeors (usually overland). Poor detection of precipitation at this stage results in either missed-rain or false-rain biases. The second stage involves utilizing a precipitation retrieval algorithm to convert the measured microwave brightness temperatures to rain rate. The ability of the algorithm to estimate the precipitation at this stage is contained in the hit bias.

For each grid's rainfall estimate that originates from a single or multiple sensors, the nature, structure, and type of errors are analyzed in detail. The spatial and temporal rainfall estimates and error variability are analyzed independently. Finally, the amount of error per grid contributed to the final level-3 product is quantitatively described for each precipitation source. For the purpose of comparison across sensors, the seasonal accumulated error components were normalized by the number of grid boxes to compute a sensor error contribution at the gridbox scale.

4. Results and discussion

The results of this study are organized into four sections: the temporal and spatial characteristics of the precipitation, correlation and scalar measures of precipitation estimates from different sensors, the spatial and temporal characteristics of error components, and the magnitude of error contribution from different sensors. The results presented in Figs. 5–14 (described in greater detail below) provide a relatively comprehensive picture of the nature of multisensor satellite precipitation estimates. To facilitate the presentation, the results are grouped and summarized based on season (winter, spring, summer, and fall), type of sensor, and error components.

a. Temporal and spatial precipitation distribution

Figure 5 shows 1) the temporal variation of accumulated precipitation from MW and IR sensors along with the reference (MRMS) accumulations (Figs. 5a,b) and 2) the spatial distribution of percent bias over the United States (Figs. 5c,d). To highlight the impact of quality-controlling the MRMS radar data using the RQI, results are presented for both the high-quality radar data (Figs. 5a,c) and the non-quality-controlled data (Figs. 5b,d). The MW-estimated accumulated precipitation over the United States is very similar to the MRMS estimates apart from moderate overestimation at the end of 2013. However, the IR-based estimates appear to significantly overestimate precipitation accumulations relative to the reference, particularly during peak accumulation periods. As discussed previously, PMW observations are more directly linked to precipitation properties than IR observations. Consequently, the IR overestimations may be attributed to cold cirrus clouds that are associated with low IR brightness temperatures and are thus assigned high rainfall rates by the retrieval algorithm.

The performance of both the MW and IR products appears worse in the absence of the radar quality-control condition (Fig. 5b). This highlights the importance of quality controlling the reference data prior to utilizing it for precipitation validation studies. However, performing sufficient quality control on the reference data is an often overlooked step in precipitation validation studies. The spatial percentage bias plots display high positive biases (satellite overestimation) in the winter and moderate (in summer and fall) positive biases over the northern and central eastern parts of the United States, respectively along with significant negative biases (satellite underestimation) over the Southwest during summer and fall. During spring, there is significant underestimation in the northeastern part of the United States. Without applying the RQI threshold, significant overestimation would have been inferred over the coastal and western mountainous regions. These inferred satellite overestimates are likely the result from radar-based underestimates arising from radar beam blockage (particularly over the complex terrain regions) and beam overshooting (over both coastal and mountainous regions), which generally occurs at far ranges from the radar site, or when higher elevation angles must be utilized to compensate for terrain obstructions.

Figure 6 displays time series of spatially accumulated precipitation over regions covered by different MW sensors along with the corresponding IR and MRMS estimates. In all locations, IR overestimates precipitation during the warm season. Focusing on the passive MW sensors, TMI consistently overestimates the peak precipitation regimes. The overestimate is probably caused by the fact that the TMI rain retrieval algorithm is biased toward higher rainfall rates that are characteristic for the region of its primary focus. SSMIS-*F17* and SSMIS-*F18* also tend to overestimate precipitation accumulations in the peak accumulation periods. On the other hand, MHS and *MetOp-B* capture both the temporal trend and magnitude of the accumulated precipitation fairly well, except for some minor underestimation associated with *MetOp-B* for the June–September time frame. Multisensor average estimates (conical and AMSU–MHS averages) also capture the rainfall trend except the overestimation at a few points.

Density-colored scatterplots of each sensor's rain estimate versus MRMS rainfall are presented in Fig. 7. All sensors' estimates share similarities on the distribution of the rainfall. All satellite sensors overestimate light

Brought to you by NOAA Central Library | Unauthenticated | Downloaded 09/27/21 03:56 PM UTC

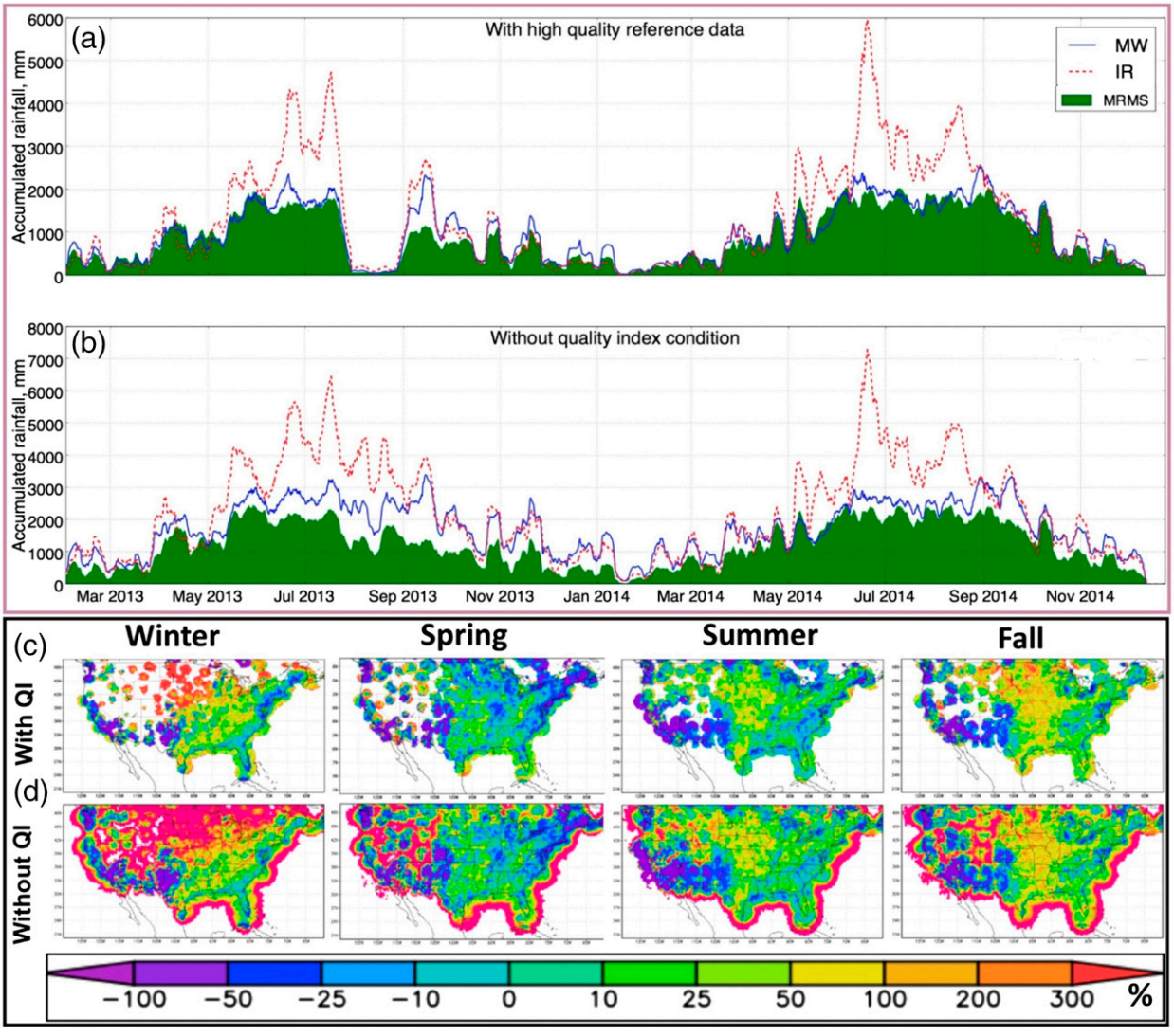

FIG. 5. Time series of rainfall estimates at 3-h time scale from all MW sensors (blue line), IR (red dotted line), and radar (MRMS; green shaded area) spatially averaged over the region where MW observation is available for the period of 2013/14 (a) with high-quality reference dataset and (b) without any quality data condition on reference dataset. (c),(d) The distribution of percent bias with and without conditioning of high quality of reference data. This figure indicates the impact of quality of reference data on validation and evaluation of satellite rainfall estimates.

rainfall and have positively skewed rainfall distributions. The correlation and percent bias show better agreement with reference data for MHS, SSMIS-*F16*, *MetOp-B*, and AMSU–MHS average rainfall estimates.

b. *Performance measures*

The performance of the satellite precipitation estimates relative to the ground reference estimates is evaluated using different correlation and scalar measures. As seen in Fig. 8, parts of the central and eastern United States are mainly characterized by positive bias in the summer and winter seasons for all sensor estimates except for SSMIS-*F17*. The bias for the northern and central plains and mountainous regions is highly positive in winter for locations where there exists high-quality radar data. The north, Midwest, New England, and western coastal regions are mostly characterized by negative bias, particularly in spring. Because of the small sample size, the spatial bias pattern associated with SSMIS-*F17* and *MetOp-B* is not as clearly defined relative to the other sensors. As mentioned earlier, TMI has positive bias because the TMI algorithm is designed for the tropical areas where the microphysics of the precipitation is different from the

Brought to you by NOAA Central Library | Unauthenticated | Downloaded 09/27/21 03:56 PM UTC

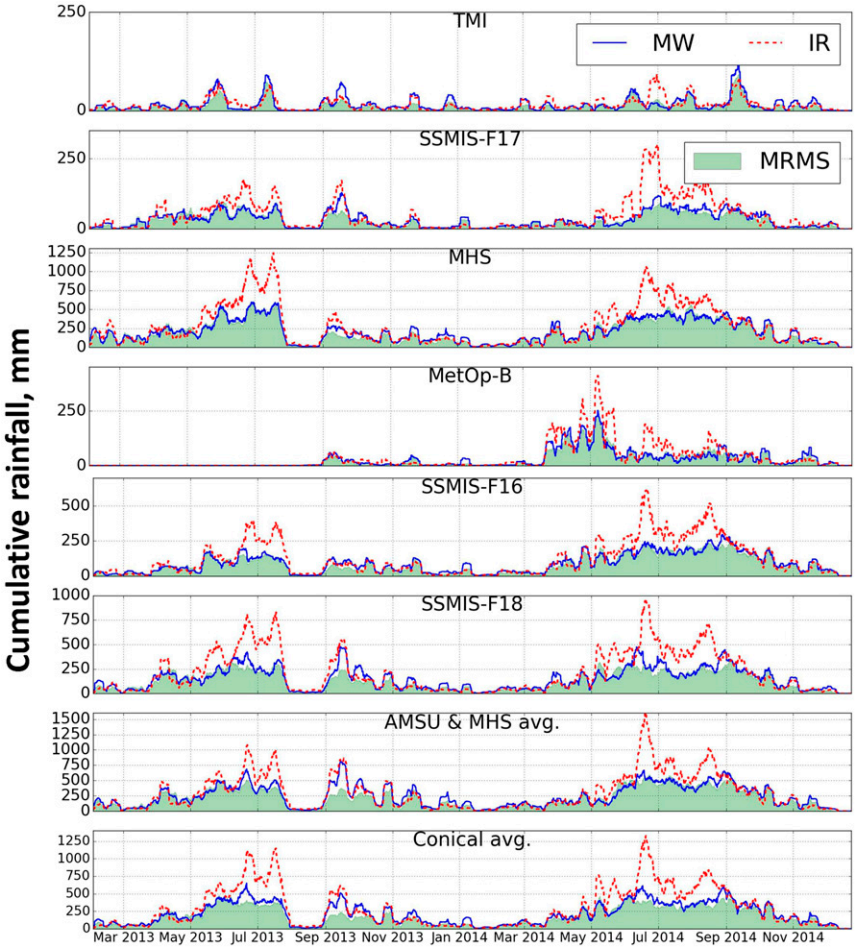

FIG. 6. Time series of rainfall estimates at 3-h time scale from MW and IR sensors with reference data (MRMS) for the period of 2013/14 over CONUS. In most cases, the satellite rainfall overestimates the rainfall and the overestimation is significant for the IR sensor.

subtropical and midlatitude regions. During spring, all products share significant similarities in that they have negative bias dominating most of the regions of the CONUS, such as the West Coast and the East Coast, Midwest, and northern regions. In fact, the underestimation during this season is mainly attributed to missed precipitation that may be caused by snow cover on the ground. In the West, orographic and shallow precipitation structure could also cause some of the biggest retrieval errors. Satellites often look straight through the shallow liquid water path of orographic storms. On the other hand, during the summer and fall season, most of the sensor estimates have positive bias in the central and eastern parts of the United States. The IR has significant positive bias over the northern part of the CONUS. The overestimation is generally traced to false precipitation (Fig. 10, described in greater detail below), possibly due to poorly calibrated IR estimates.

To further evaluate the agreement between the satellite and reference datasets, correlation coefficient, Nash–Sutcliffe efficiency, and root-mean-square error (RMSE) were computed and are displayed in Fig. 9. The Nash–Sutcliffe efficiency (from $-\infty$ to 1) is a normalized measure that compares the mean square error of the rainfall estimated by the satellite to the variance of the reference data (MRMS). It represents a form of noise-to-signal ratio, comparing the average variability of the satellite rainfall estimates to the MRMS. The MW precipitation estimates are strongly correlated with MRMS data with a correlation coefficient above 0.8 (0.86 for SSMIS-*F18* and 0.96 for MHS). The correlation coefficient for the corresponding IR estimates in regions where MW coverage is available ranges between 0.6 and 0.75. For all MW sensors, the Nash–Sutcliffe efficiency is positive (0.49 for SSMIS-*F18* and 0.8 for MHS). In both correlation measures MHS displays the best

Brought to you by NOAA Central Library | Unauthenticated | Downloaded 09/27/21 03:56 PM UTC

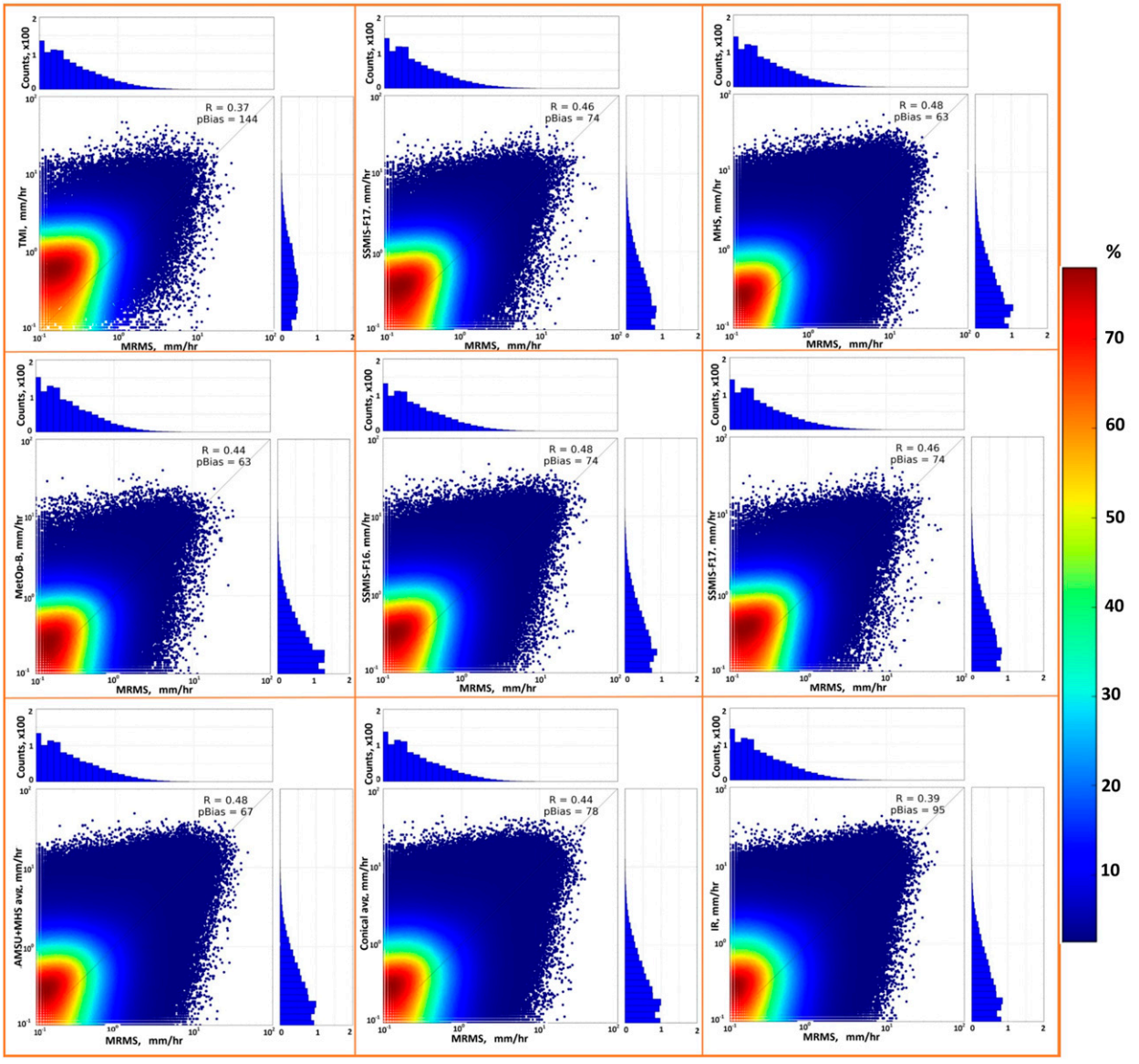

FIG. 7. Scatterplots of rain rates from different sensors vs reference rainfall (mm h^{-1}) with marginal histograms. The colors show a normalized density as percent of the max count. In each plot, the correlation coefficient R and the percent bias are displayed at the upper-right corner. Note that the type of sensor is shown on the y axis.

performance among all MW sensors. The RMSE measures the magnitude of the error, and a smaller RMSE indicates that the satellite precipitation estimate is closer to the reference estimate. Similar to the correlation measures, the RMSE for passive MW sensors is lower than the IR RMSE; however, TMI has a comparable RMSE to the IR estimates (same as Fig. 6, top).

c. *Error structures in MW and IR sensors*

To better track the error sources associated with multisensor precipitation estimates, it is important to examine both the characteristics and magnitude of the error components. As seen in Fig. 10, the magnitude of all error components for MW sensors is smaller than the IR during the study period. In case of the passive MW sensors, the dominant error sources are the missed-rain and hit biases. The missed-rain bias in passive MW radiometers is largely due to the poor spatial (due to diffraction) and temporal (only on board low-Earth-orbiting platforms) sampling frequencies. The hit bias is related to the ability of the retrieval algorithm to relate the brightness temperature T_b to the amount of rain. This relationship can yield over- or underestimation depending on the precipitation rate, the nature of the

Brought to you by NOAA Central Library | Unauthenticated | Downloaded 09/27/21 03:56 PM UTC

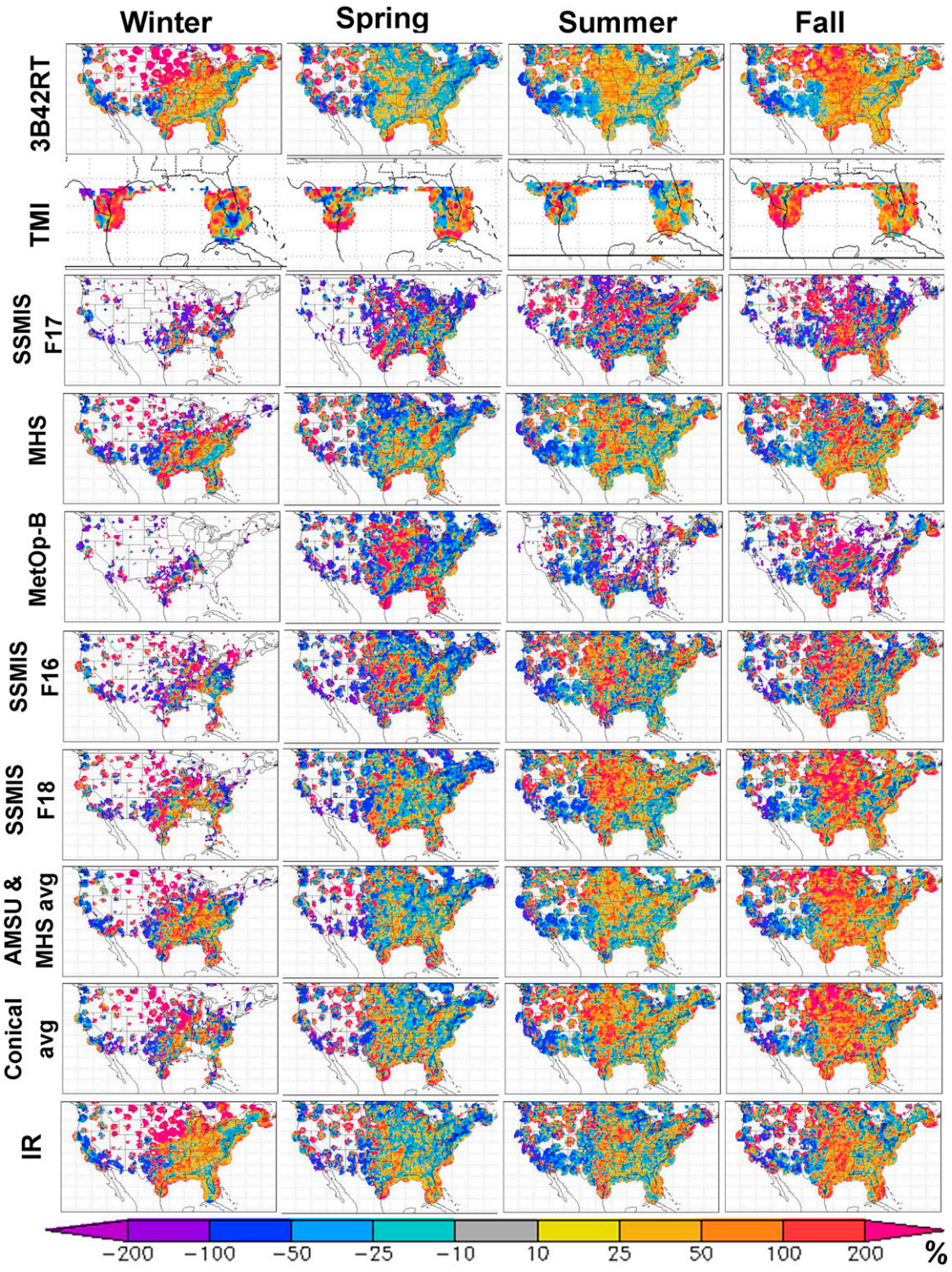

FIG. 8. Percent bias of rainfall estimates from different sensors over the United States during 2013/14.

Brought to you by NOAA Central Library | Unauthenticated | Downloaded 09/27/21 03:56 PM UTC

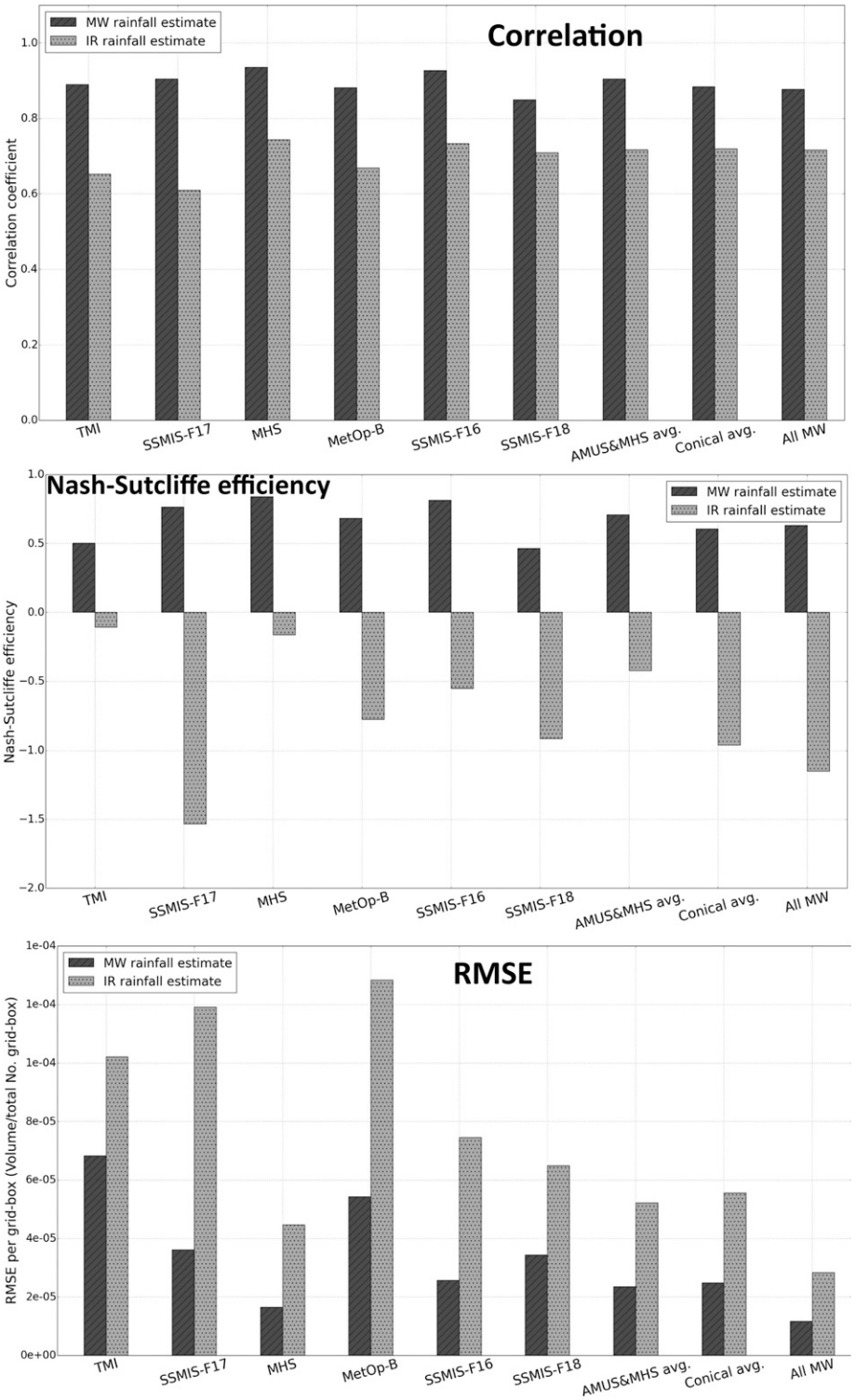

FIG. 9. Correlation and scalar measures between rainfall estimates of various sensors and reference data (MRMS QPE): (top) correlation coefficient, (middle) Nash–Sutcliffe efficiency, and (bottom) RMSE. For the purpose of comparison, the RMSE is normalized by the number of grid boxes.

Brought to you by NOAA Central Library | Unauthenticated | Downloaded 09/27/21 03:56 PM UTC

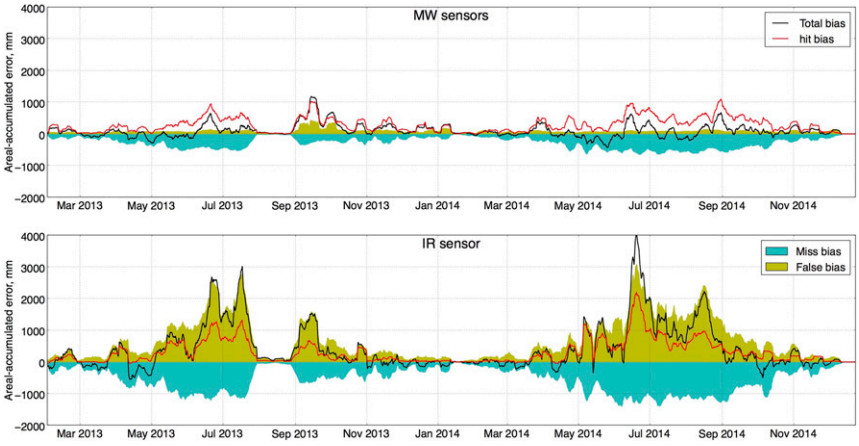

FIG. 10. Time series of error components at 3-h time scale for (top) MW and (bottom) IR rainfall estimates, spatially averaged over CONUS. To reduce visual cluttering, a 7-day (56 observations) moving average is applied. The total bias (black line) is the sum of all independent error components: the hit bias (red line), miss rain (light blue shading), and false rain (light green shading).

precipitation (vertical extent), and the microphysics (ice phase). But in this case, overestimation is particularly noteworthy during the high rainfall seasons of summer and fall. In the case of IR, all the error components significantly contribute to the total error. Particularly, the false precipitation in the case of IR is 2–10 times larger than the MW. This highlights the limitations of the IR retrieval algorithm both in detecting and quantifying precipitation. The magnitude of the error is generally related to the magnitude of the precipitation (see Fig. 6), and this finding is consistent with results from earlier studies (e.g., Huffman 1997; Gebregiorgis and Hossain 2014).

Figures 11 and 12 present the spatial distribution of percentage of occurrence of each error component of the MW and IR estimates for the winter and summer seasons, respectively. In addition to the three error components, the figures also present the percentage of ''no error'' condition that reflects the cases when both satellite and ground products see no rain. Regarding the spatial distribution of the occurrence of error components, there are common features shared by all sensors. During the winter, false precipitation is observed mainly in northern parts of the United States, whereas missed precipitation is a problem in most of the study domain, but is particularly significant in the eastern portions of the domain, including both the northern and southeastern United States. The IR estimate shows slightly higher sampling frequency in the central and eastern parts of the United States. In addition, the occurrence of hit bias mainly covers the East Coast region. For the summer season, the frequency of missed-precipitation and hit bias is widespread across the region, with high percentages in the Northeast, Southeast, and Midwest. The missed-precipitation bias over summer is particularly high over the Intermountain West and the Southeast. This phenomenon could result from shallow orographic precipitation (over the Intermountain West) and (tropical) warm-rain precipitation (over the Southeast). Both these types of precipitation events have low concentrations of ice-phase hydrometeors and thus are difficult to detect by PMW retrieval algorithms because of the low magnitude ice-phase scattering signal (Shige et al. 2013). Moreover, as mentioned above, the space–time rainfall structure, which covers small regions and then disappears quickly, is a challenge for PMW because of the infrequent sampling time. On top of this, the narrower coverage of the MW sensors and PR is another problem to handle the short-lived nature of convective bursts during the TRMM era.

d. Error contribution from MW and IR sensors

The main objective of this study is to identify the source of errors and to quantify their contributions to the total error in the TRMM level-3 product. These results are presented based on season and sensor type. As seen in Fig. 13, the contribution of the error components from MW and IR sensors are quantified per grid. The error for the IR estimate is computed both for regions where the corresponding MW estimate is available and regions where the MW estimate is unavailable, that is, where IR is used in the 3B42RT product. The latter scenario is obviously included in the merged 3B42RT product to gap fill in regions where MW observations are missing.

Regarding MW precipitation estimates, the major error sources comprising the total error are positive hit

Brought to you by NOAA Central Library | Unauthenticated | Downloaded 09/27/21 03:56 PM UTC

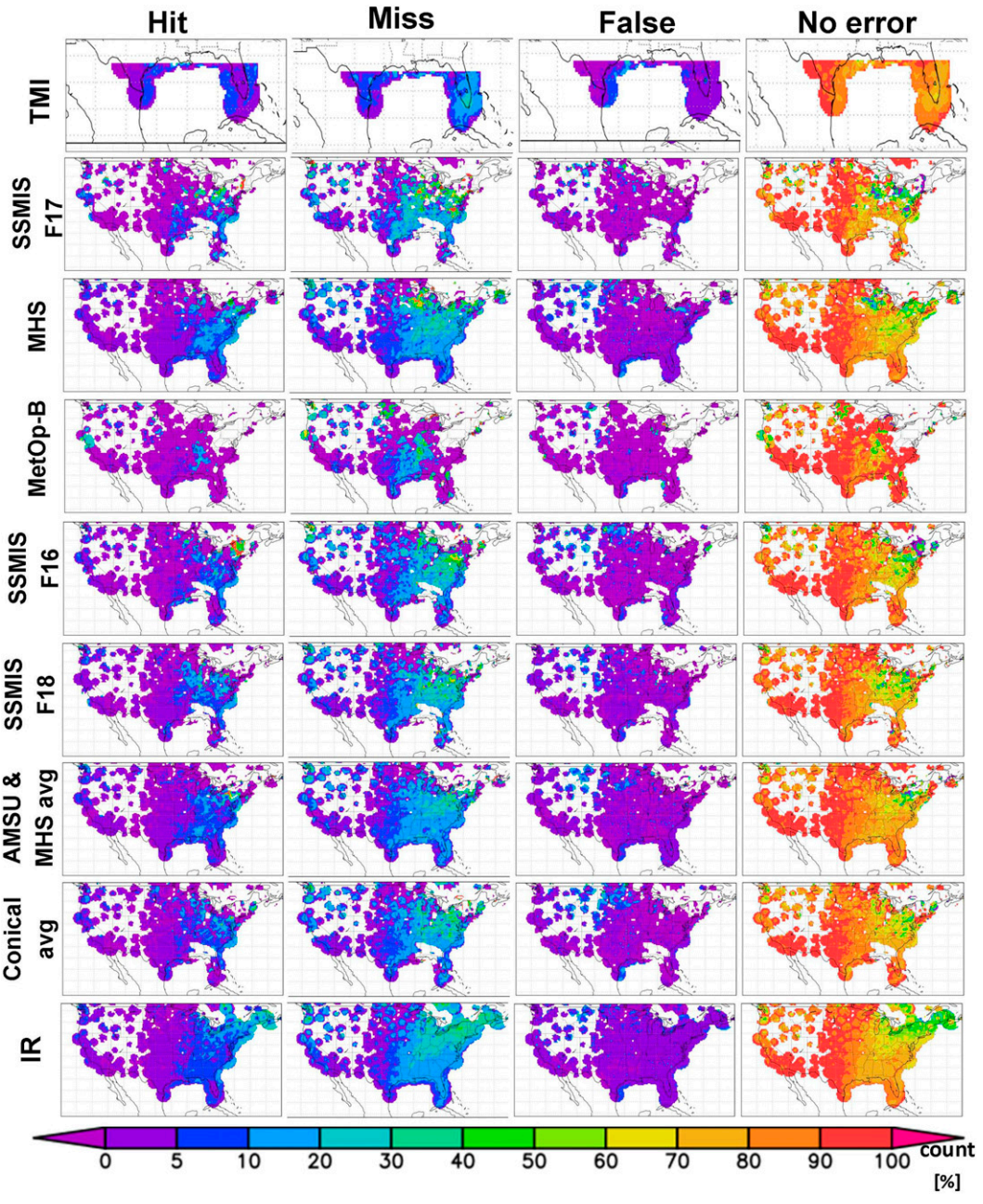

FIG. 11. Percentage of occurrence of hit, miss, and false errors during the winter season of 2013/14. Note that the sum of the percentage of hit, miss, false, and no error add up to 100.

and missed-rain biases. In all seasons, the contribution of positive hit and missed-rain bias is comparable in magnitude but of opposite sign. Hence they can compensate for each other, making the total bias smaller than some of the component errors (e.g., during spring and summer seasons). The false-rain bias is less than the other two error components. The largest false-rain bias from MW sensors occurs during the winter season, likely due to the impact of frozen/snow-covered surfaces on the retrieved MW T_b. The biases from IR estimates are computed from two different regions: 1) from regions where MW estimate is available, that is, the IR estimates are not used in 3B42RT; and 2) from regions where MW observations are not available, that is, the IR estimates are used in 3B42RT. In the case of IR precipitation estimates, like PMW, the hit and missed-rain biases are the main contributors to the total error for regions where there are no MW observations. In MW regions, the

Brought to you by NOAA Central Library | Unauthenticated | Downloaded 09/27/21 03:56 PM UTC

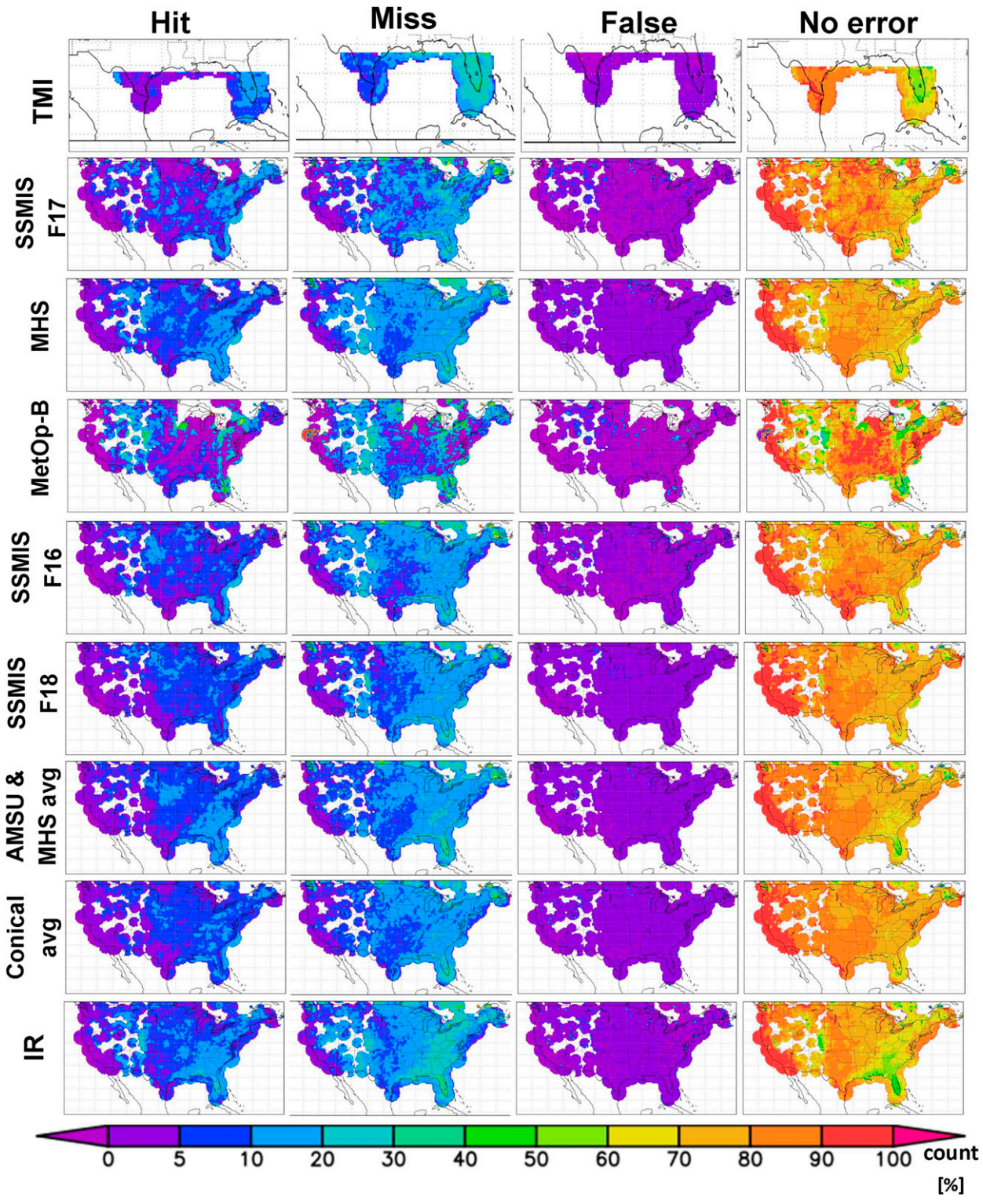

FIG. 12. As in Fig. 11, but for the summer season of 2013/14.

Brought to you by NOAA Central Library | Unauthenticated | Downloaded 09/27/21 03:56 PM UTC

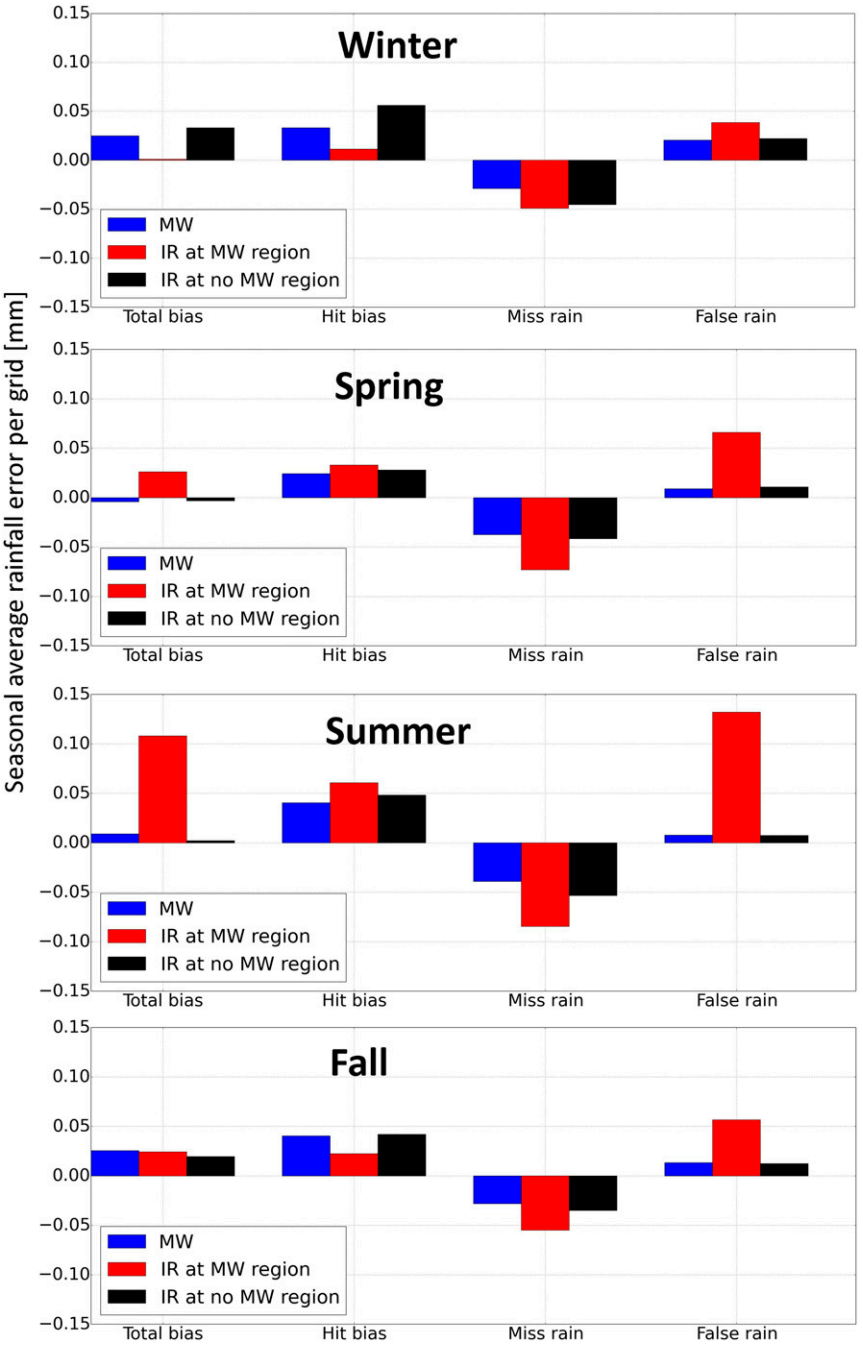

FIG. 13. The contribution of error components from MW and IR sensors to the merged level-3 TRMM product (3B42RT) per grid box. To obtain the true total error contribution of each sensor, the value should be multiplied by the total number of grid box covered by the sensor.

false-rain bias from IR estimates is significantly high, particularly during the summer, and low during the winter.

To further examine the sources of bias, the error contribution from each individual MW sensor/combinations of MW sensors is displayed in Fig. 14. The contribution of error components to the total error can be ranked (from largest to smallest magnitude) as missed-rain, positive hit bias, and false-rain biases for all MW or combination of MW sensors. However, the magnitude of the error varies among the sensor types in different seasons. For example, during the winter

Brought to you by NOAA Central Library | Unauthenticated | Downloaded 09/27/21 03:56 PM UTC

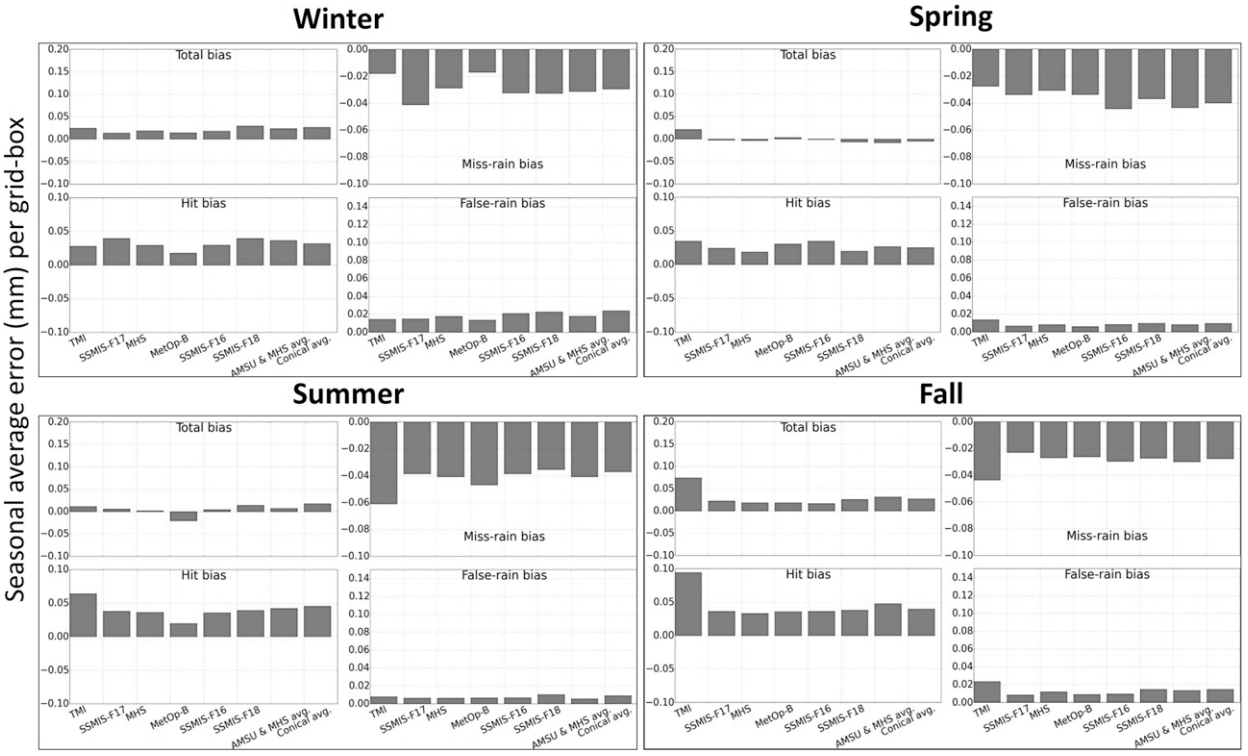

FIG. 14. The contribution of error components from the MW sensors used in level-3 TRMM product. The *y* axis shows the seasonal average error (mm) normalized by the number of grids.

season, the minimum hit bias originates from the *MetOp-B* and the maximum originates from the SSMIS-*F17* and SSMIS-*F18*. For the same season, the minimum missed-rain bias comes from *MetOp-B* and the maximum from SSMIS-*F17*; the false-rain bias minimum is from *MetOp-B* and the maximum is from SSMIS-*F18*. During the spring, the MHS and SSMIS-*F16* are the minimum and maximum error contributors per unit area, respectively, for both hit and missed-rain biases. During summer, *MetOp-B* and TMI produce the lowest and highest biases per grid, respectively. The false-rain bias contribution to the total bias diminishes for all sensors during both spring and summer (likely due to a decrease in snow-covered surfaces). In the fall, TMI produces the largest error biases for all error components per unit area, whereas the remaining sensors contribute roughly the same magnitude of error. In summary, the current version of the 3B42RT algorithm appears to have lower biases related to false precipitation than were associated with previous versions of the algorithm. Specifically, earlier studies (Tian et al. 2009; Gebregiorgis and Hossain 2014) reported that 3B42RT had substantial false-rain biases overland, particularly in the Midwest. This study reveals that the false-rain bias contribution to the total bias is minimal and that missed-rain bias remains a major source of error in the 3B42RT product.

5. Conclusions

This study investigates the characteristics of satellite precipitation error by decomposing the error components based on sensor type and eventually traces and quantifies the magnitude of errors produced by MW and IR sensors. The 3B42RT precipitation estimates obtained from TMI, SSMIS-*F16*, SSMIS-*F17*, SSMIS-*F18*, MHS, *MetOp-B*, AMSU–MHS average, conical average, and IR are investigated. Ground-based radar data (MRMS) are utilized as reference data to evaluate the error characteristics of the aforementioned satellite precipitation estimates for the period from 2 January 2013 to 31 December 2014. The major findings of this study can be summarized as follows:

1) Since precipitation estimates from ground-based weather radars can be influenced by several error sources (Kirstetter et al. 2015), the reference data should be quality controlled prior to being used to evaluate the performance of satellite precipitation estimates. Validation without data quality assessment could lead to the product being misunderstood and result in incorrect conclusions. Therefore, before

Brought to you by NOAA Central Library | Unauthenticated | Downloaded 09/27/21 03:56 PM UTC

using the reference data (MRMS) for the purposes of validation and analysis of satellite precipitation estimates, a threshold of RQI (specifically requiring the RQI to be its maximum value) has been imposed to ensure the highest possible reference quality. Comparisons with and without the RQI threshold demonstrate that this quality-control step has a noticeable impact on the analysis and interpretations of results. Ensuring the accuracy, timeliness, completeness, and consistency of data before using for any application ensures that satellite precipitation data users and algorithm developers have a common understanding of what the data represent.

2) The magnitude of error associated with the IR precipitation estimates is considerably higher than the error associated with the MW estimates. Specifically, in the case of false precipitation, the magnitude of the IR error is 2–10 times higher than the MW, the IR missed-rain bias is double that of the MW, and both precipitation estimates exhibit nearly the same magnitude of positive hit bias (with a few exceptions) during the study period (2013/14). Positive hit bias and missed precipitation are the major sources of error for MW estimates, whereas all three error components play a significant role in building the total bias in the IR estimates. This result is expected as MW-observed quantities (i.e., T_b) are more physically linked to precipitation properties than IR-observed quantities. In general, the false-rain bias associated with the current MW retrieval algorithm is lower in magnitude than the false-rain bias associated with previous versions of the algorithm analyzed in earlier studies (e.g., Tian et al. 2009). However, there is still plenty of room for improvement, as substantial missed-precipitation and hit biases still exist.
3) Another important finding is that the contribution of error from MW sensors varies seasonally. For example, TMI contributes the highest missed-rain and positive hit biases per grid during the summer and fall seasons. Regarding missed precipitation, SSMIS-*F17* and SSMIS-*F16* are the major error contributors during the winter and spring, respectively. On the other hand, MHS and *MetOp-B* produce the smallest portion of hit and missed-rain biases. Sample size and area coverage are the most important factors that need to be considered in the performance analysis of sensors. The other aspect, which needs to be considered, is the type of sensors (imagers or sounders). Both sensors have different scanning patterns: imagers are conically scanning sensors while sounders are cross track. Both cross-track and conical-scanning sensors use different retrievals. A more comprehensive evaluation of a given sensor's performance is possible for sensors with high sampling frequency and high spatial coverage. Because of the limited sampling coverage for *MetOp-B* (less than 5% in most parts of the CONUS), its capability to estimate precipitation in different conditions (e.g., diverse geographic setups and different precipitation systems) could not be verified. However, MHS, which has better spatial coverage and sampling frequency, contributes the minimum error to the final level-3 product.
4) To get more insight of the error structure created within individual sensors, it is helpful to decompose the total bias into its components. These error components sometimes add up to build the total bias (such as negative hit and missed-rain biases or positive hit and false-rain biases) and sometimes cancel each other out. In general, the errors originating from IR sensors (false- and missed-rain biases) are often associated with the screening stage of the algorithm process (rain/no-rain detection capability). But in terms of the hit bias (error associated with retrieval stage of the algorithm), both MW and IR sensors exhibit closer performance.

In summary, this study has detailed some of the main error characteristics inherited in multisensor gridded satellite precipitation estimates and has expressed these error characteristics as functions of space, time, season, and sensor type. In addition to segregating precipitation estimates based on the source of the estimates, it is also important to segregate precipitation estimates on the basis of geophysical (such as topography and surface types, land use and land cover, etc.) and precipitation (such as precipitation type, i.e., convective or stratiform) parameters. Given the fine spatial resolution of its level-3 products, the IMERG is the best satellite precipitation product to test the aforementioned concept. Therefore, future research will focus on evaluating IMERG products on the basis of sensor type and various geophysical and precipitation parameters.

Acknowledgments. This work was supported by NASA project Grants NNX15AL36G and NNX13AF84G. The authors also acknowledge the two anonymous reviewers and the editor for their comprehensive, insightful, and constructive comments during the review process of this manuscript.

REFERENCES

Adler, R. F., and A. J. Negri, 1988: A satellite infrared technique to estimate tropical convective and stratiform rainfall. *J. Appl. Meteor.*, **27**, 30–51, doi:10.1175/1520-0450(1988)027<0030:ASITTE>2.0.CO;2.

Brought to you by NOAA Central Library | Unauthenticated | Downloaded 09/27/21 03:56 PM UTC

——, C. Kidd, G. Petty, M. Morissey, and H. M. Goodman, 2001: Intercomparison of global precipitation products: The third Precipitation Intercomparison Project (PIP–3). *Bull. Amer. Meteor. Soc.*, **82**, 1377–1396, doi:10.1175/1520-0477(2001)082<1377:IOGPPT>2.3.CO;2.

Arkin, P. A., and B. Meisner, 1987: The relationship between large-scale convective rainfall and cold cloud over the Western Hemisphere during 1982–84. *Mon. Wea. Rev.*, **115**, 51–74, doi:10.1175/1520-0493(1987)115<0051:TRBLSC>2.0.CO;2.

Carr, N., and Coauthors, 2015: The influence of surface and precipitation characteristics on TRMM TMI rainfall retrieval uncertainty. *J. Hydrometeor.*, **16**, 1596–1614, doi:10.1175/JHM-D-14-0194.1.

Chen, S., and Coauthors, 2013: Evaluation and uncertainty estimation of NOAA/NSSL next-generation National Mosaic Quantitative Precipitation Estimation product (Q2) over the continental United States. *J. Hydrometeor.*, **14**, 1308–1322, doi:10.1175/JHM-D-12-0150.1.

Crum, T. D., R. L. Alberty, and D. W. Burgess, 1993: Recording, archiving, and using WSR-88D data. *Bull. Amer. Meteor. Soc.*, **74**, 645–653, doi:10.1175/1520-0477(1993)074<0645:RAAUWD>2.0.CO;2.

Ebert, E. E., J. E. Janowiak, and C. Kidd, 2007: Comparison of near-real-time precipitation estimates from satellite observations and numerical models. *Bull. Amer. Meteor. Soc.*, **88**, 47–64, doi:10.1175/BAMS-88-1-47.

Ferraro, R. R., 1997: SSM/I derived global rainfall estimates for climatological applications. *J. Geophys. Res.*, **102**, 16 715–16 735, doi:10.1029/97JD01210.

——, and Coauthors, 2005: NOAA operational hydrological products derived from the advanced microwave sounding unit. *IEEE Trans. Geosci. Remote Sens.*, **43**, 1036–1049, doi:10.1109/TGRS.2004.843249.

Gebregiorgis, A. S., and F. Hossain, 2011: How much can a priori hydrologic model predictability help in optimal merging of satellite precipitation products? *J. Hydrometeor.*, **12**, 1287–1298, doi:10.1175/JHM-D-10-05023.1.

——, and ——, 2013: Performance evaluation of merged satellite rainfall products based on spatial and seasonal signatures of hydrologic predictability. *Atmos. Res.*, **132–133**, 223–238, doi:10.1016/j.atmosres.2013.05.003.

——, and ——, 2014: Estimation of satellite precipitation error variance using readily available geophysical features. *IEEE Trans. Geosci. Remote Sens.*, **52**, 288–304, doi:10.1109/TGRS.2013.2238636.

——, and ——, 2015: How well can we estimate error variance of satellite precipitation data across the world? *Atmos. Res.*, **154**, 39–59, doi:10.1016/j.atmosres.2014.11.005.

Gottschalck, J., J. Meng, M. Rodell, and P. Houser, 2005: Analysis of multiple precipitation products and preliminary assessment of their impact on Global Land Data Assimilation System land surface states. *J. Hydrometeor.*, **6**, 573–598, doi:10.1175/JHM437.1.

Hollinger, J. P., J. L. Pierce, and G. A. Poe, 1990: SSM/I instrument evaluation. *IEEE Trans. Geosci. Remote Sens.*, **28**, 781–790, doi:10.1109/36.58964.

Hong, Y., R. F. Adler, F. Hossain, S. Curtis, and G. J. Huffman, 2007a: A first approach to global runoff simulation using satellite rainfall estimation. *Water Resour. Res.*, **43**, W08502, doi:10.1029/2006WR005739.

——, ——, and G. J. Huffman, 2007b: Satellite remote sensing for global landslide monitoring. *Eos, Trans. Amer. Geophys. Union*, **88**, 357–358, doi:10.1029/2007EO370001.

Hou, A. Y., G. Skofronick-Jackson, C. D. Kummerow, and J. M. Shepherd, 2008: Global precipitation measurement. *Precipitation: Advances in Measurement, Estimation, and Precipitation.* S. C. Michaelides, Ed., Springer, 131–169.

——, and Coauthors, 2014: The Global Precipitation Measurement Mission. *Bull. Amer. Meteor. Soc.*, **95**, 701–722, doi:10.1175/BAMS-D-13-00164.1.

Hsu, K., X. Gao, S. Sorooshian, and H. V. Gupta, 1997: Precipitation Estimation from Remotely Sensed Information Using Artificial Neural Networks. *J. Appl. Meteor.*, **36**, 1176–1190, doi:10.1175/1520-0450(1997)036<1176:PEFRSI>2.0.CO;2.

Huffman, G. J., 1997: Estimates of root-mean-square random error contained in finite sets of estimated precipitation. *J. Appl. Meteor.*, **36**, 1191–1201, doi:10.1175/1520-0450(1997)036<1191:EORMSR>2.0.CO;2.

——, and D. T. Bolvin, 2015: Real-time TRMM Multi-Satellite Precipitation Analysis data set documentation. NASA TRMM Doc., 47 pp. [Available online at http://pmm.nasa.gov/sites/default/files/document_files/3B4XRT_doc_V7.pdf.]

——, and Coauthors, 2007: The TRMM Multisatellite Precipitation Analysis (TMPA): Quasi-global, multiyear, combined-sensor precipitation estimates at fine scales. *J. Hydrometeor.*, **8**, 38–55, doi:10.1175/JHM560.1.

——, R. F. Adler, D. T. Bolvin, and E. J. Nelkin, 2010: The TRMM Multi-satellite Precipitation Analysis (TMPA). *Satellite Rainfall Applications for Surface Hydrology*, F. Hossain and M. Gebremichael, Eds., Springer, 3–22, doi:10.1007/978-90-481-2915-7_1.

——, D. T. Bolvin, and E. J. Nelkin, 2015: Integrated Multi-satellitE Retrievals for GPM (IMERG) Technical Documentation. NASA/GSFC Code 612 Tech. Doc., 48 pp. [Available online at http://pmm.nasa.gov/sites/default/files/document_files/IMERG_doc.pdf.]

Iguchi, T., T. Kozu, R. Meneghini, J. Awaka, and K. Okamoto, 2000: Rain-profiling algorithm for the TRMM Precipitation Radar. *J. Appl. Meteor.*, **39**, 2038–2052, doi:10.1175/1520-0450(2001)040<2038:RPAFTT>2.0.CO;2.

Joyce, R. J., J. E. Janowiak, P. A. Arkin, and P. Xie, 2004: CMORPH: A method that produces global precipitation estimates from passive microwave and infrared data at high spatial and temporal resolution. *J. Hydrometeor.*, **5**, 487–503, doi:10.1175/1525-7541(2004)005<0487:CAMTPG>2.0.CO;2.

Kidd, C. K., D. R. Kniveton, M. C. Todd, and T. J. Bellerby, 2003: Satellite rainfall estimation using combined passive microwave and infrared algorithms. *J. Hydrometeor.*, **4**, 1088–1104, doi:10.1175/1525-7541(2003)004<1088:SREUCP>2.0.CO;2.

Kirstetter, P. E., and Coauthors, 2012: Toward a framework for systematic error modeling of spaceborne precipitation radar with NOAA/NSSL ground radar-based National Mosaic QPE. *J. Hydrometeor.*, **13**, 1285–1300, doi:10.1175/JHM-D-11-0139.1.

——, H. Andrieu, B. Boudevillain, and G. Delrieu, 2013: A physically based identification of vertical profiles of reflectivity from volume scan radar data. *J. Appl. Meteor. Climatol.*, **52**, 1645–1663, doi:10.1175/JAMC-D-12-0228.1.

——, J. J. Gourley, Y. Hong, J. Zhang, S. Moazamigoodarzi, C. Langston, and A. Arthur, 2015: Probabilistic precipitation rate estimates with ground-based radar networks. *Water Resour. Res.*, **51**, 1422–1442, doi:10.1002/2014WR015672.

Kubota, T., S. Shige, K. Aonashi, and K. Okamoto, 2009: Development of nonuniform beamfilling correction method in

Brought to you by NOAA Central Library | Unauthenticated | Downloaded 09/27/21 03:56 PM UTC

rainfall retrievals for passive microwave radiometers over ocean using TRMM observations. *J. Meteor. Soc. Japan*, **87A**, 153–164, doi:10.2151/jmsj.87A.153.

Kummerow, C., W. Barnes, T. Kozu, J. Shiue, and J. Simpson, 1998: The Tropical Rainfall Measuring Mission (TRMM) sensor package. *J. Atmos. Oceanic Technol.*, **15**, 809–817, doi:10.1175/1520-0426(1998)015<0809:TTRMMT>2.0.CO;2.

Maddox, R. A., J. Zhang, J. J. Gourley, and K. W. Howard, 2002: Weather radar coverage over the contiguous United States. *Wea. Forecasting*, **17**, 927–934, doi:10.1175/1520-0434(2002)017<0927:WRCOTC>2.0.CO;2.

McCollum, J. R., and R. R. Ferraro, 2003: Next generation of NOAA/NESDIS TMI, SSM/I, and AMSR-E microwave land rainfall algorithms. *J. Geophys. Res.*, **108**, 8382, doi:10.1029/2001JD001512.

Sapiano, M. R. P., and P. A. Arkin, 2009: An intercomparison and validation of high-resolution satellite precipitation estimates with 3-hourly gauge data. *J. Hydrometeor.*, **10**, 149–166, doi:10.1175/2008JHM1052.1.

Shibata, A., K. Imaoka, and T. Koike, 2003: AMSR/AMSR-E level 2 and 3 algorithm developments and data validation plans of NASDA. *IEEE Trans. Geosci. Remote Sens.*, **41**, 195–203, doi:10.1109/TGRS.2002.808320.

Shige, S., S. Kida, H. Ashiwake, T. Kubota, and K. Aonashi, 2013: Improvement of TMI rain retrievals in mountainous areas. *J. Appl. Meteor. Climatol.*, **52**, 242–254, doi:10.1175/JAMC-D-12-074.1.

Smith, E. A., and Coauthors, 1998: Results of the WetNet PIP-2 project. *J. Atmos. Sci.*, **55**, 1483–1536, doi:10.1175/1520-0469(1998)055<1483:ROWPP>2.0.CO;2.

Stephens, G. L., and Coauthors, 2002: The *CloudSat* mission and the A-Train: A new dimension of space-based observations of clouds and precipitation. *Bull. Amer. Meteor. Soc.*, **83**, 1771–1790, doi:10.1175/BAMS-83-12-1771.

Sun, N., and F. Weng, 2008: Evaluation of Special Sensor Microwave Imager/Sounder (SSMIS) environmental data records. *IEEE Trans. Geosci. Remote Sens.*, **46**, 1006–1016, doi:10.1109/TGRS.2008.917368.

Tang, L., Y. Tian, and X. Lin, 2014: Validation of precipitation retrievals over land from satellite-based passive microwave sensors. *J. Geophys. Res. Atmos.*, **119**, 4546–4567, doi:10.1002/2013JD020933.

Tian, Y., and C. D. Peters-Lidard, 2007: Systematic anomalies over inland water bodies in satellite-based precipitation estimates. *Geophys. Res. Lett.*, **34**, L14403, doi:10.1029/2007GL030787.

——, and ——, 2010: A global map of uncertainties in satellite-based precipitation measurements. *Geophys. Res. Lett.*, **37**, L24407, doi:10.1029/2010GL046008.

——, ——, B. J. Choudhury, and M. Garcia, 2007: Multitemporal analysis of TRMM based satellite precipitation products for land data assimilation applications. *J. Hydrometeor.*, **8**, 1165–1183, doi:10.1175/2007JHM859.1.

——, and Coauthors, 2009: Component analysis of errors in satellite-based precipitation estimates. *J. Geophys. Res.*, **114**, D24101, doi:10.1029/2009JD011949.

——, C. D. Peters-Lidard, R. F. Adler, T. Kubota, and T. Ushio, 2010: Evaluation of GSMaP precipitation estimates over the contiguous United States. *J. Hydrometeor.*, **11**, 566–574, doi:10.1175/2009JHM1190.1.

Turk, F. J., and S. D. Miller, 2005: Toward improved characterization of remotely sensed precipitation regimes with MODIS/AMSR-E blended data techniques. *IEEE Trans. Geosci. Remote Sens.*, **43**, 1059–1069, doi:10.1109/TGRS.2004.841627.

——, G. D. Rohaly, J. Hawkins, E. A. Smith, F. S. Marzano, A. Mugnai, and V. Levizzani, 1999: Meteorological applications of precipitation estimation from combined SSM/I, TRMM and infrared geostationary satellite data. *Microwave Radiometry and Remote Sensing of the Earth's Surface and Atmosphere*, P. Pampaloni and S. Paloscia, Eds., VSP International Science Publishers, 353–363.

Vila, D., R. Ferraro, and R. Joyce, 2007: Evaluation and improvement of AMSU precipitation retrievals. *J. Geophys. Res.*, **112**, D20119, doi:10.1029/2007JD008617.

Weng, F., L. Zhao, R. Ferraro, G. Poe, X. Li, and N. Grody, 2003: Advanced microwave sounding unit cloud and precipitation algorithms. *Radio Sci.*, **38**, 8068, doi:10.1029/2002RS002679.

Zhang, J., Y. Qi, K. Howard, C. Langston, and B. Kaney, 2011: Radar quality index (RQI)—A combined measure of beam blockage and VPR effects in a national network. *IAHS Publ.*, **351**, 388–393.

——, and Coauthors, 2016: Multi-Radar Multi-Sensor (MRMS) quantitative precipitation estimation: Initial operating capabilities. *Bull. Amer. Meteor. Soc.*, **97**, 621–638, doi:10.1175/BAMS-D-14-00174.1.

Brought to you by NOAA Central Library | Unauthenticated | Downloaded 09/27/21 03:56 PM UTC